

Combined plasmon-resonance and photonic-jet effect in the THz wave scattering by dielectric rod decorated with graphene strip

Cite as: J. Appl. Phys. **126**, 023104 (2019); <https://doi.org/10.1063/1.5093674>

Submitted: 23 February 2019 . Accepted: 18 June 2019 . Published Online: 11 July 2019

Sergii V. Dukhopelnykov , Ronan Sauleau , Maria Garcia-Viguera , and Alexander I. Nosich 



View Online



Export Citation



CrossMark



 **Alluxa** YOUR OPTICAL COATING PARTNER  **DOWNLOAD THE LIDAR WHITEPAPER**

Combined plasmon-resonance and photonic-jet effect in the THz wave scattering by dielectric rod decorated with graphene strip

Cite as: J. Appl. Phys. 126, 023104 (2019); doi: 10.1063/1.5093674

Submitted: 23 February 2019 · Accepted: 18 June 2019 ·

Published Online: 11 July 2019



Sergii V. Dukhopelnykov,^{1,a)} Ronan Sauleau,² Maria Garcia-Vigueras,³ and Alexander I. Nosich¹

AFFILIATIONS

¹Laboratory of Micro and Nano Optics, Institute of Radio-Physics and Electronics NASU, Kharkiv 61085, Ukraine

²Institute of Electronics and Telecommunications of Rennes, Université de Rennes 1, Rennes 35042, France

³Institute of Electronics and Telecommunications of Rennes, Institut Nationale de Science Appliqué, Rennes 35042, France

Note: This paper is part of the Special Topic on Dielectric Nanoresonators and Metamaterials.

^{a)}dukh.sergey@gmail.com

ABSTRACT

We consider the scattering of an H-polarized plane wave by an infinite dielectric rod with a conformal graphene strip of arbitrary angular width, placed at the rod rear side. Our analysis is based on the hypersingular integral equation for the current induced on the strip. Discretization of this equation is carried out by the Nystrom-type method, which has a guaranteed convergence. This meshless trusted computational instrument enables us to plot the dependences of the absorption cross section and the total scattering cross section on the strip angular width and the frequency, in a wide range from 1 GHz to 6 THz. We concentrate our analysis on studying the interplay between the broadband photonic-jet effect of the dielectric rod and the reasonably high-Q resonances on the plasmon modes of the graphene strip. It is found that as the photonic jet becomes brighter with higher frequencies, the plasmon-mode resonances become more intensive as well.

Published under license by AIP Publishing. <https://doi.org/10.1063/1.5093674>

I. INTRODUCTION

A circular dielectric rod is known to produce a specific near-field effect called a “photonic jet” provided that its relative dielectric permittivity is less than 4, and the rod radius is at least twice larger than the wavelength.^{1,2} The larger the radius, the narrower and brighter the photonic jet. This is, in fact, a sort of an imperfect focusing effect, nonresonant and, therefore, explained by the geometrical optics for optically large rods, although for mesoscale ones diffraction is also essential, according to Ref. 3. Note that this imperfect focusing can be improved by making the circular rod “discrete,” i.e., concentrically layered, with stepwise dielectric permittivity mimicking the Luneburg lens. Photonic jets on various dielectric scatterers were reported in Refs. 4–7. On the other hand, a strip made of graphene is able to support plasmon modes in the infrared and THz ranges of frequencies.^{8–10} If such a strip is placed into the photonic-jet area, one can expect that two effects can be combined, thus increasing the amplitude of the field in the vicinity of the rod without increasing its radius.

Guided by these considerations, we are going to analyze the scattering and absorption of a THz range H-polarized plane wave by a circular dielectric rod with a graphene strip located at the rear side of rod—see Fig. 1.

For solving this problem, we combine the Maxwell boundary-value problem with the Kubo model of graphene conductivity. Here, we consider the graphene as a zero-thickness layer with a complex surface electron conductivity defined by the chemical potential, frequency, temperature, and relaxation time.¹¹ Note that the thickness of the graphene monolayer or a small stack of them is so small, 1–2 nm, that the assumption of zero thickness is perfectly valid even in the X-ray range. The famous hexagonal honeycomb fine in-plane structure of graphene has a characteristic size of 10 nm and hence graphene’s surface conductivity can be safely considered isotropic in the THz and even in the visible range. Nonlocal effects in the conductivity can be neglected if the size of graphene samples is larger than 100 nm.

Graphene strips have already attracted attention in the THz science community as attractive and easily manufactured components of plasmonic waveguides, antennas, and sensors.^{12–14} Apart from

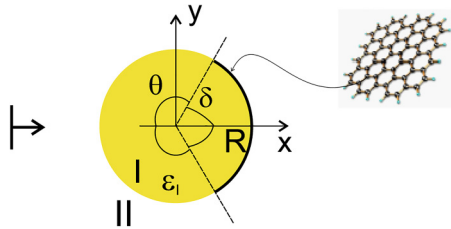


FIG. 1. Cross section of a circular dielectric rod with a partial graphene cover.

commercial codes, their modeling has been done with several convergent methods: regularizing method-of-moments, the Riemann-Hilbert Problem (RHP) method, and Nystrom-type discretization with Chebyshev quadratures.^{15–21} Application of these mathematically grounded methods allows finding the solutions to the considered problems with controlled accuracy within a reasonable time of computation.

Single flat strip scattering was studied in Refs. 8–10 and its waveguiding properties in Ref. 15. Plasmon-assisted resonances in the scattering and absorption by infinite and finite gratings of coplanar graphene strips under normal and inclined incidence were analyzed in Refs. 15–19. Focusing ability of a parabolic graphene reflector in the free space was considered in Ref. 20. Still most frequently graphene is placed on top of the dielectric layer, which provides better mechanical rigidity. Such a combination of graphene with dielectric objects results in the interplay between the resonances associated with each part of the whole configuration. This, for instance, was demonstrated in Ref. 21 where the THz wave scattering and absorption by a graphene strip grating embedded into a dielectric slab was analyzed with the aid of regularizing method-of-moments. Curved graphene-dielectric configurations studied so far have been mainly restricted to fully covered circular dielectric rods.^{22–25} The arbitrary dielectric rod, fully covered with graphene, was analyzed with boundary integral equation in Ref. 26. The authors of Ref. 27 considered a finite-width graphene strip attached to the surface of the arbitrary dielectric rod using quasi-static approximations. In our work, we build on the preliminary studies presented in the conference papers.^{28,29}

The remaining part of the paper is organized as follows. In Sec. II, we reduce the problem to a dual-series equation and then to a hypersingular integral equation, which is discretized in Sec. III. In Sec. IV, we obtain an approximate formula for the resonance values of the graphene strip angular width as a function of the frequency and rod’s parameters. In Sec. V, we present numerical results and discuss them. Section VI contains the conclusions.

II. DERIVATION OF HYPERSINGULAR INTEGRAL EQUATION

Consider the H-polarized time-harmonic ($e^{-i\omega t}$) plane wave incident on a circular dielectric cylinder (rod), the outer boundary of which is partially covered with a conformal strip of graphene placed symmetrically to the incident wave propagation direction. The cross section of such a scatterer by the coordinate plane $z = 0$ is presented in Fig. 1, where the cylindrical coordinates (r, φ, z) are

co-axial with the rod. Here, R is the radius of the rod and 2δ is the angular width of the graphene strip, so that $2\theta = 2\pi - 2\delta$ is the angular width of the slot. The H-polarized field has electromagnetic field components of $(E_r, E_\phi, 0)$ and $(0, 0, H_z)$.

As the H_z field does not depend on z , we obtain the following two-dimensional find the function $H_z(r, \phi)$, which satisfies (i) the Helmholtz equation with the wavenumber $k^{I,II}$ for all $r \neq R$,

$$\Delta H_z(r, \phi) + (k_{I,II})^2 H_z(r, \phi) = 0, \quad (1)$$

(ii) the dual boundary condition at $r = R$: on the graphene arc, $L = \{r = R, |\phi| \leq \delta\}$, this is

$$E_\phi^I + E_\phi^{II} = 2ZZ_0(H_z^I - H_z^{II}) \text{ and } E_\phi^I = E_\phi^{II}, \quad (2)$$

while on the slot arc, $S = \{r = R, |\phi - \pi| \leq \theta\}$, this is

$$H_z^I = H_z^{II} \text{ and } E_\phi^I = E_\phi^{II}, \quad (3)$$

(iii) the Sommerfeld radiation condition at infinity, and (iv) the local power finiteness.

Here, $ZZ_0 = 1/\sigma$ is the graphene surface impedance, σ is the surface conductivity, Z_0 is the impedance of the free space, index I (II) is assigned to the inside (outside) domain filled in with a dielectric of the permittivity $\epsilon_{I,II}$ and $k_{I,II} = (\omega/c)\sqrt{\epsilon_{I,II}}$, where c is the speed of light in vacuum.

The given incident wave, $H_z^{inc} = e^{ik_\parallel x}$, propagates along the positive direction of the x axis. The total field can be presented as the Fourier series,

$$H_z^{(I,II)} = \begin{cases} H_z^{inc} + \sum_{-\infty}^{+\infty} C_{II,n} H_n(k^{II} r) e^{in\varphi} / H'_n(k^{II} R), & r \geq R, \\ \sum_{-\infty}^{+\infty} C_{I,n} J_n(k^I r) e^{in\varphi} / J'_n(k^I R), & r < R. \end{cases} \quad (4)$$

Here, $J_n(\zeta)$ and $H_n(\zeta)$ are the Bessel and Hankel first kind functions of integer order n , prime means a derivative of the functions, and $C_{(I,II),n}$ is unknown coefficients, which should be found. Such a field satisfies the Helmholtz equation and the radiation condition.

Using the boundary conditions (2) and (3) at $r = R$, we derive the following dual series equation:

$$\begin{cases} \sum_{n=-\infty}^{+\infty} A_n W_n e^{in\varphi} - iZ \sum_{n=-\infty}^{+\infty} A_n e^{in\varphi} = f(\varphi), & |\varphi| < \delta, \\ \sum_{n=-\infty}^{+\infty} A_n e^{in\varphi} = 0, & \delta \leq |\varphi| \leq \pi. \end{cases} \quad (5)$$

The field expansion coefficients in (4) depend on A_n as

$$\begin{aligned} C_{I,n} &= \sqrt{\epsilon_I} W_n (A_n - i^n J'_n H_n / H'_n + i^n J_n), \\ C_{II,n} &= \sqrt{\epsilon_{II}} W_n (A_n - i^n J'_n H_n / H'_n + i^n J_n) - i^n J'_n, \end{aligned} \quad (6)$$

$$W_n = \left[\sqrt{\epsilon_I} J_n (J'_n)^{-1} - \sqrt{\epsilon_{II}} H_n (H'_n)^{-1} \right]^{-1}, \quad (7)$$

and the right-hand part function is

$$f(\varphi) = \sum_{n=-\infty}^{\infty} i^n J'_n H_n (H'_n)^{-1} W_n e^{in\varphi} - \sum_{n=-\infty}^{\infty} i^n J_n W_n e^{in\varphi}. \quad (8)$$

Introduce the function

$$v(\varphi) = \sum_{n=-\infty}^{+\infty} A_n e^{in\varphi}. \quad (9)$$

From the bottom line of (5), we can find that $v(\varphi) = 0$, hence

$$A_n = (2\pi)^{-1} \int_{-\delta}^{\delta} v(\varphi) e^{-in\varphi} d\varphi, \quad n = 0, \pm 1, \pm 2, \dots \quad (10)$$

Then, with the aid of parametric representations²⁸ of the integral operators with the hyper-singular and logarithmic kernels, we obtain from the top line of (5) an integral equation over the interval $(-\delta, \delta)$

$$\begin{aligned} & -\frac{B_1}{2\pi} \left(h.f.p. \int_{-\delta}^{\delta} \frac{v(\psi)}{2\sin^2[(\psi - \varphi)/2]} d\psi \right) \\ & - B_2 \pi^{-1} \int_{-\delta}^{\delta} v(\psi) \ln \left| \sin \frac{\psi - \varphi}{2} \right| d\psi \\ & + \frac{W_0 - 2B_2 \ln 2}{2\pi} \int_{-\delta}^{\delta} v(\psi) d\psi, \\ & - \pi^{-1} \int_{\delta}^{\delta} K(\psi, \varphi) v(\psi) d\psi - iZv(\varphi) = f(\varphi), \end{aligned} \quad (11)$$

where *h.f.p.* denotes Hadamard's finite part

$$K(\psi, \varphi) = \sum_{n=1}^{\infty} (W_n - B_1|n| - B_2|n|^{-1}) \cos n(\varphi - \psi), \quad (12)$$

$$B_1 = 1/kR(\epsilon_I + \epsilon_{II}), \quad B_2 = -\frac{1}{2}kR(\epsilon_I^2 + \epsilon_{II}^2)(\epsilon_I + \epsilon_{II})^{-2}. \quad (13)$$

Further, on introducing new notations $f(\varphi) = f(t_0)$, where $|\varphi| < \delta$ and $t_0 = \varphi/\delta$, and also $t = \psi/\delta$, we transform this integral equation into the equation over the standard interval $(-1, 1)$,

$$\begin{aligned} & -iZ\gamma(t_0)\delta\sqrt{1-t_0^2} - \frac{B_1}{\pi} \left(h.f.p. \int_{-1}^1 \gamma(t) \frac{\sqrt{1-t^2}}{(t-t_0)^2} dt \right) \\ & - B_2\delta^2\pi^{-1} \int_{-1}^1 \gamma(t) \ln|t-t_0|\sqrt{1-t^2} dt \\ & + \delta^2\pi^{-1} \int_{-1}^1 \gamma(t)\sqrt{1-t^2}K(t_0, t)dt = f(t_0), \end{aligned} \quad (14)$$

with a smooth kernel $K(t, t_0) = \sum_{n=1}^{\infty} (W_n - B_1|n| - B_2|n|^{-1}) \cos[n\delta(t - t_0)]$. Note that the local power finiteness condition is fulfilled at the strip edges as the function $v(\psi)$, which is the electric current on the graphene strip, has the form $v(t) = \delta\gamma(t)(1 - t^2)^{1/2}$, where the function $\gamma(t)$ remains finite at the strip edges, i.e., if $t \rightarrow \pm 1$.

III. DISCRETIZATION AND CONVERGENCE

In the discretization of the integral equation (14), the unknown function $\gamma(t)$ is substituted with the interpolating polynomial $\gamma^{N-1}(t)$, and the integrals within the equation are replaced with interpolation quadrature formulas.³⁰ Here, the equation kernels should also be replaced with their interpolating polynomials having the same nodes, which are the zeros of the Chebyshev second kind polynomials, t_{0p} ,

$$\begin{aligned} & iZ\delta\gamma^{N-1}(t_{0q})(1 - (t_{0q})^2) + \frac{B_1}{N+1} \sum_{\substack{p=1 \\ p \neq q}}^N \gamma^{N-1}(t_{0p})(1 - (t_{0p})^2) \frac{1 - (-1)^{q+p}}{(t_{0q} - t_{0p})^2} - B_1 \frac{(N+1)\gamma^{N-1}(t_{0q})}{2} - \frac{B_2}{N+1} \delta^2 \sum_{p=1}^N \gamma^{N-2}(t_{0p})[1 - (t_{0p})^2] \\ & \times \left[\ln 2 + 2 \sum_{s=1}^N T_s(t_{0p})T_s(t_{0q})/s + (-1)^{p+q}/(2N+2) \right] - 2\delta^2/(N+1) \sum_{p=1}^N \gamma(t_{0p})(1 - (t_{0p})^2)K(t_{0q}, t_{0p}) = -f(t_{0q}), \quad q = 1, \dots, N. \end{aligned} \quad (15)$$

Denoting $x_q = \gamma^{N-1}(t_{0q})$, we rewrite this set as

$$Z_q x_q + \sum_{p=1}^N A_{qp} x_p = b_q, \quad q = 1, \dots, N, \quad (16)$$

where $b_q = -f(t_{0q})$, $Z_q = i\delta Z(1 - t_{0q}^2)$ are known, and the elements of the matrix take the form

$$A_{qq} = \left\{ -\frac{1}{2}B_1(N+1)^2 - B_2\delta^2[1 - (t_{0q})^2] \times \left[\ln 2 + 2 \sum_{s=1}^N T_s(t_{0q})T_s(t_{0q})/s + (-1)^{2q}/(2N+2) \right] - 2\delta^2(1 - t_{0q}^2)K(t_{0q}, t_{0q}) \right\} / (N+1), \quad (17)$$

$$\begin{aligned} A_{qp} = & \left\{ B_1[1 - (t_{0p})^2] \frac{1 - (-1)^{q+p}}{(t_{0q} - t_{0p})^2} - B_2\delta^2[1 - (t_{0p})^2] \times \left[\ln 2 + 2 \sum_{s=1}^N T_s(t_{0p})T_s(t_{0q})/s + (-1)^{p+q}/(2N+2) \right] \right. \\ & \left. - 2\delta^2[1 - (t_{0p})^2]K(t_{0q}, t_{0p}) \right\} / (N+1) \quad \text{if } q \neq p, \end{aligned} \quad (18)$$

where $T_s(t_{0q})$ stands for the Chebyshev polynomial of the first kind of the order s .

The obtained matrix equation has strong diagonal predominance. The convergence of the solution of (16) with $N \rightarrow \infty$ is guaranteed by the theorems of approximation of hypersingular operators with the aid of quadratures.³⁰ The validation of the constructed algorithm has been performed by the comparison with RHP method results available in Ref. 31 for the limit case of $\varepsilon = 1$ and $Z = \text{const}$. As both methods are convergent, the agreement is within an arbitrary number of digits, controlled by the order of discretization.

IV. GRAPHENE CONDUCTIVITY AND PLASMON RESONANCES

Today, the most widely recognized model of the electromagnetic properties of graphene monolayer is the Kubo formalism.¹¹ It tells that the graphene surface conductivity is a sum of the intraband and interband terms, $\sigma(\omega) = \sigma_{\text{intra}} + \sigma_{\text{inter}}$, where the second term heavily dominates from the statics to the optical frequencies. Then,

$$Z(\omega) \approx (Z_0 \sigma_{\text{intra}})^{-1} = (1/\tau - i\omega)/(Z_0 c_1), \quad (19)$$

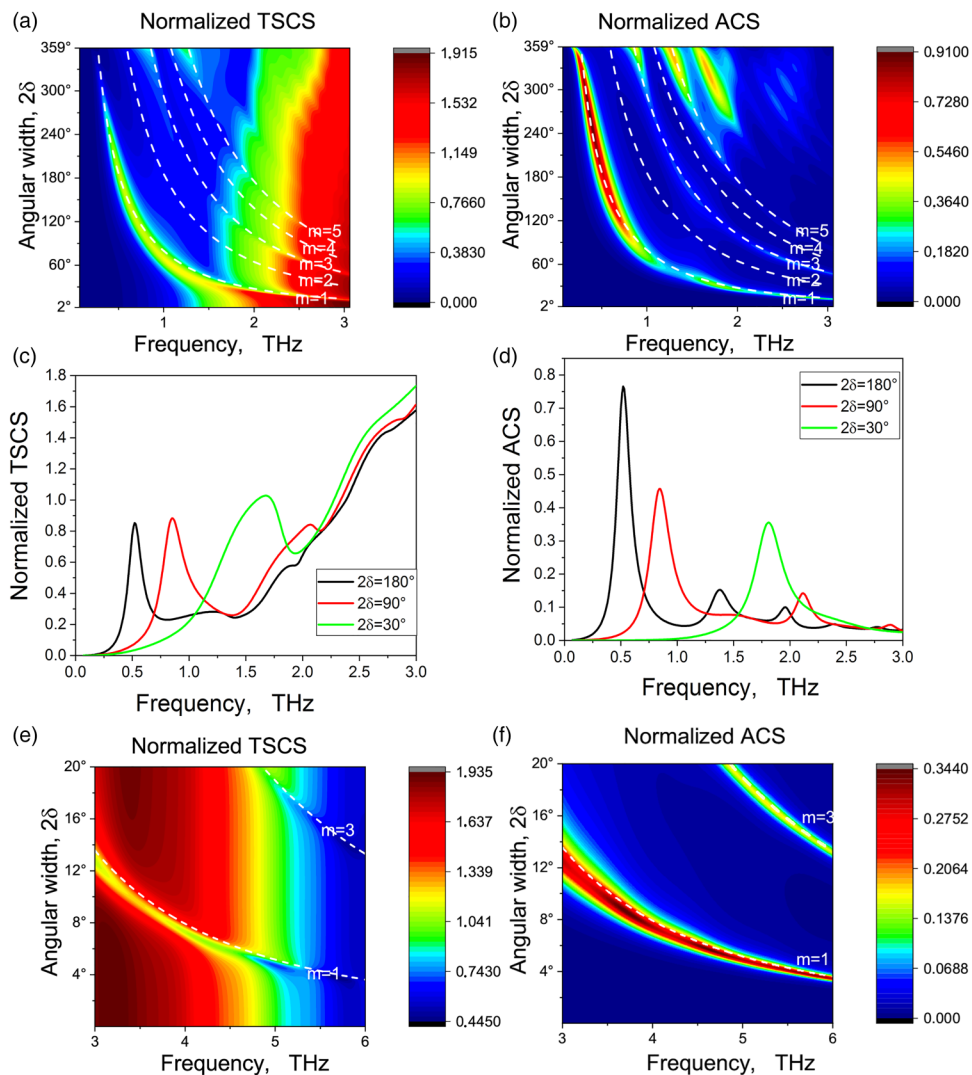


FIG. 2. Color maps of TSCS (a) and ACS (b) vs two variables: the angular width of graphene strip and the frequency. Panels (c) and (d) show cross sections of maps on panels (a) and (b) at the fixed angular widths of graphene strip, 2δ . Panels (e) and (f) show zoomed-in areas of the right-bottom corners of panels (a) and (b), respectively. The dielectric rod radius is $R = 50 \mu\text{m}$, its relative dielectric constant is $\varepsilon_l = 2.4$, and the graphene parameters are explained in the text.

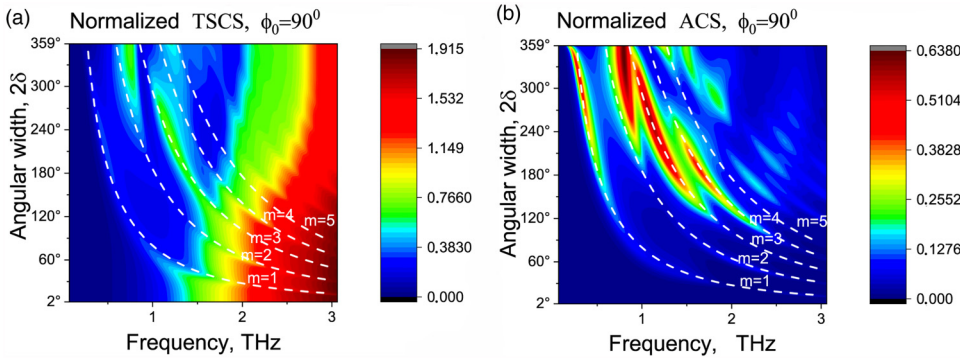


FIG. 3. The same in Figs. 2(a) and 2(b), however for the graphene-strip arc rotated by 90° around rod's axis.

where

$$c_1 = q_e^2 k_B T (\pi \hbar^2)^{-1} \{ \mu_c (k_B T)^{-1} + 2 \ln(1 + \exp(-\mu_c (k_B T)^{-1})) \} \quad (20)$$

is a value that is independent of the frequency, q_e is the electron charge, k_B is the Boltzmann constant, T is the temperature, \hbar is the reduced Planck constant, τ is the electron relaxation time, and μ_c is the chemical potential.

The plasmon modes (i.e., the natural oscillations) of a strip of graphene are commonly viewed as the modes of a Fabry-Perot resonator working on the plasmon surface wave,^{8–10} which bounces between the strip edges. This is an empiric model, which is however well supported by the full-wave computations and experiments. Assuming that the graphene layer is infinite and its curvature can be neglected, the complex propagation constant of the plasmon wave can be found as

$$\gamma_{plas}^2(\omega) \approx k^2(\epsilon_I + \epsilon_{II}) \left[\frac{1}{2} - Z^2(\epsilon_I + \epsilon_{II}) \right]. \quad (21)$$

Then, the approximate empiric equation for the transverse plasmon modes on the strip of the width $2\delta R$ is obtained as

$$\sin(\text{Re}\gamma_{plas} 2\delta R + \psi) \approx 0. \quad (22)$$

Here, the value of ψ is associated with the phase of the reflection coefficient of the plasmon wave from the strip edge.

Our study has shown that the best fit of the first-order plasmon-mode resonance is provided by $\psi = \pi/4$. Note that expression (21) is more accurate than Eq. (25) of Ref. 10, which can be obtained by setting $Z = 0$.

The roots of (22) determine the natural frequencies of the graphene strip plasmon modes P_m , whose fields are symmetric and anti-symmetric with respect to the strip middle point. They can be assigned odd ($m = 1, 3, \dots$) and even indices ($m = 2, 4, \dots$), respectively. In view of the fact that the graphene surface impedance is a function of the frequency given by (19), the resonance values of the graphene strip angular width are obtained as follows:

$$2\delta \approx (\pi m - \psi) \omega^{-2} Z_0 c c_1 [(\epsilon_I + \epsilon_{II}) R]^{-1}. \quad (23)$$

As demonstrated by the numerical results presented in Sec. V, this equation is in excellent agreement with full-wave computations.

V. NUMERICAL RESULTS

Here, we present and discuss several characteristics, which depend on the frequency and the size of the graphene strip. These are the far-field scattering pattern,

$$D(\phi) = \sum_{n=-\infty}^{+\infty} C_{2,n} (-i)^n e^{in\phi} / H_n^{(1)'}(k^I R), \quad (24)$$

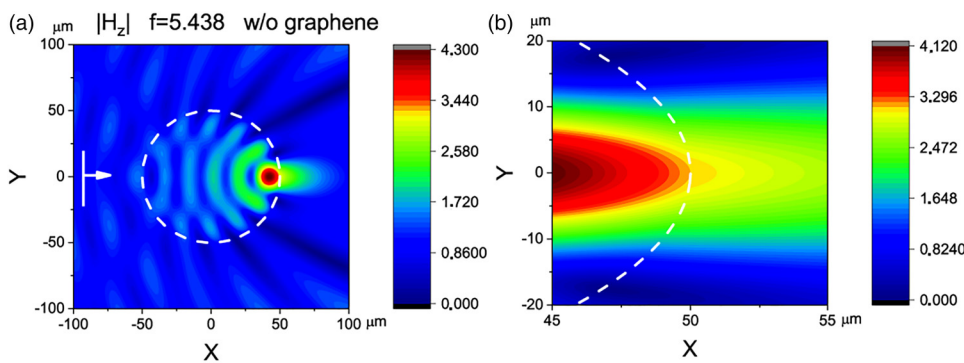


FIG. 4. Normalized near-field patterns for the 50-um rod of $\epsilon_I = 2.4$ without graphene illumination by a plane H-polarized wave at $f = 5.438$ THz. The right panel shows a zoom of a part of the left panel.

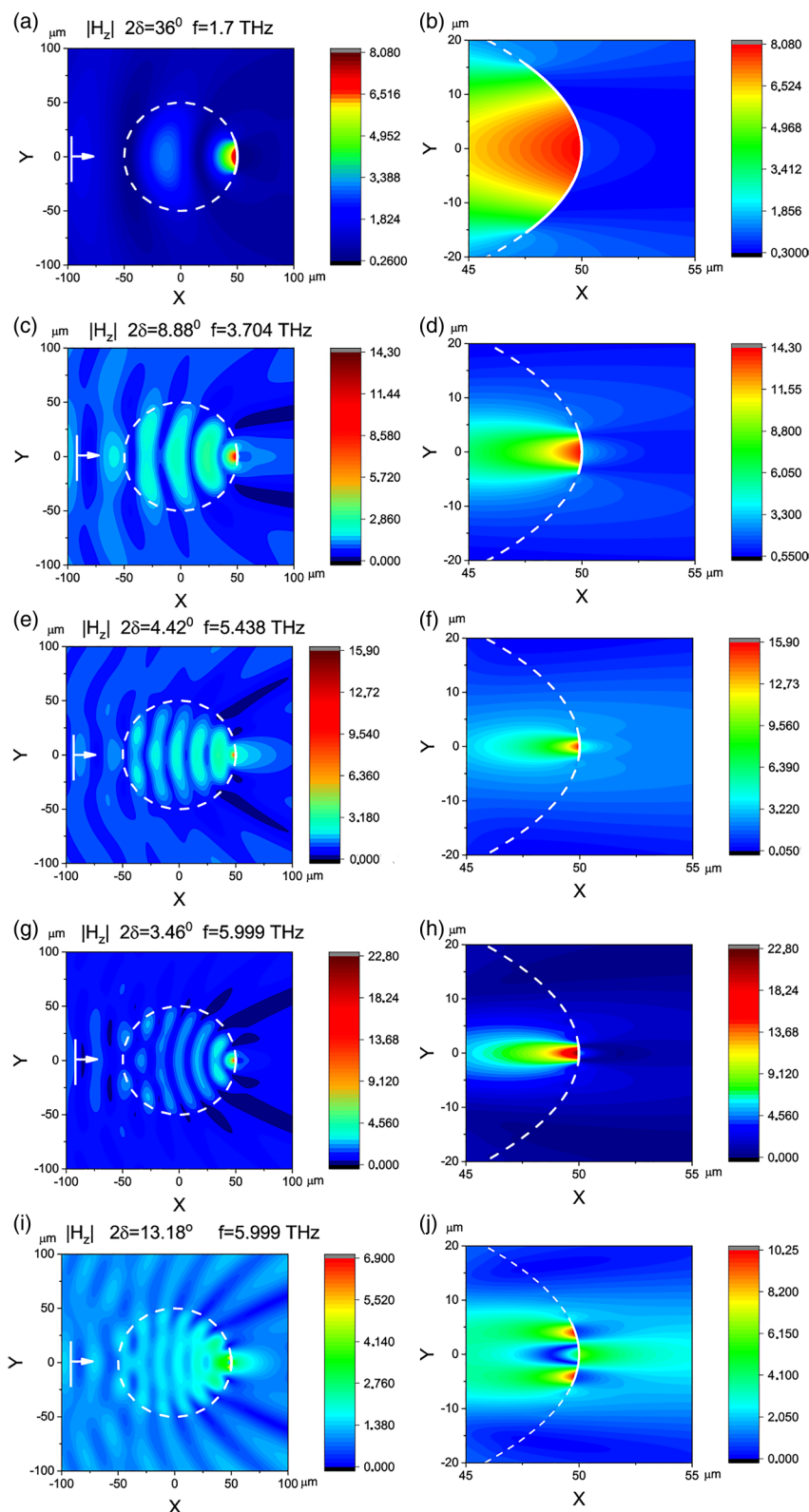


FIG. 5. The same as in Fig. 4, however for the rod with a graphene strip at its rear side, with the strip angular width and the frequency as indicated. (a) and (b) $2\delta = 36^\circ$, $f = 1.7$ THz, (c) and (d) $2\delta = 8.88^\circ$, $f = 3.704$ THz, (e) and (f) $2\delta = 4.42^\circ$, $f = 5.438$ THz, (g) and (h) $2\delta = 3.46^\circ$, $f = 5.999$ THz, (i) and (j) $2\delta = 13.18^\circ$, $f = 5.999$ THz.

and the total scattering and absorption cross sections, i.e.,

$$S_{TSCS} = (4/k_{II}) \sum_{n=-\infty}^{+\infty} |C_{2,n}|^2 |H'_n|^{-2}, \quad (25)$$

$$S_{ACS} = R \operatorname{Re} Z \int_{\alpha}^{\beta} |v(\phi)|^2 d\phi. \quad (26)$$

In computations, we normalize the cross sections by $4R$, and take $R = 50 \mu\text{m}$ and the following parameters of graphene: $\tau = 1 \text{ ps}$, $T = 300 \text{ K}$, $\mu_c = 0.5 \text{ eV}$. To clarify the effect of the graphene strip, we build color maps of total scattering cross section (TSCS) and absorption cross section (ACS) as a function of the frequency and the strip angular width (see Figs. 2 and 3). On these maps, a higher-scattering range between 2.5 and 4.5 THz is the contribution of the dielectric rod, while that of the strip shows up as narrow curved “ridges.”

On the maps, the white dashed curves are the values predicted by (23) for the orders m from 1 to 5. As visible, the odd-index curves agree well with the actual resonances on the corresponding plasmon modes of the curved graphene strip. Here, the resonances on the even-index plasmon modes are absent because these modes are “dark” in the case of symmetric strip placement. For better understanding, the plots in Figs. 2(c) and 2(d) show the sections of the maps presented on panels (a) and (b), respectively, at the fixed values of strip angular width, 2δ . In Figs. 2(e) and 2(f), we zoom in the high-frequency extensions of Figs. 2(a) and 2(b), respectively, where graphene becomes more transparent; however, the plasmon-mode resonances are still present, on the narrower strips.

The maps in Figs. 3(a) and 3(b) are similar to those in Figs. 2(a) and 2(b); however, computed for the graphene strip attached to the dielectric rod in such a way that the strip center is on the y axis of Fig. 1. Modification of our equations to arbitrary nonsymmetric strip placement needs some algebra, not presented here. In this case, the even-index plasmon modes become “bright,” i.e., the corresponding resonance peaks appear on the spectra of TSCS and ACS. As visible, their location is also well predicted by Eq. (23).

To understand why so narrow graphene strips remain strong resonant absorbers if located at the rear side of the rod, we have analyzed the near-field patterns, i.e., the portraits of the $|H_z|$ value normalized by $H_0 = 1 \text{ A/m}$. The field in Fig. 4 corresponds to the 50- μm dielectric rod without graphene strip at the frequency of 5.438 THz. Here, one can clearly see the photonic jet^{1,2} at the rod rear side.

This high-intensity field spot has its maximum inside the rod near to its boundary; at the higher frequencies, it shifts out of the rod, however, remains close to its boundary. This feature has broadband geometrical-optics character. Therefore, if a narrow graphene strip is placed on the rear side of the rod and its width is tuned to a plasmon resonance, it is illuminated more efficiently and the ACS shows a peak at the frequency of (23). Several in-resonances near fields are shown in Fig. 5. The solid white arcs indicate graphene strips and the dashed arcs—the dielectric rod boundary. In all cases, the graphene strip is placed on the rear side of the rod and hence near the photonic-jet area.

Panels (a)–(h) correspond to the first order plasmon P_1 ($m = 1$) and panels (i) and (j) to the third-order plasmon P_3 ($m = 3$). As already mentioned that if the incident plane wave propagates along the x axis, then the even-order plasmon modes of the strip remain

“dark” (not excited) because their fields are orthogonal to such excitation. It is clearly seen that the peak field value gets higher for the narrower strips, apparently because the photonic jet becomes brighter.

Here, the resonance on P_1 yields a three times greater increment in the near-field amplitude than on P_3 at the same frequency of 5.999 THz. This indicates inherently that the Q-factor of P_3 is three times lower than the Q-factor of P_1 that is in line with inverse- m behavior of Q-factors of modes in the other Fabry-Perot resonators.

Note also that if the strip material is a perfect electric conductor ($Z = 0$), then the plasmon modes are absent and the discussed resonance phenomenon does not exist.

VI. CONCLUSION

We have presented the results of the accurate study of the scattering and absorption of an H-polarized THz plane wave by a graphene-strip decorated circular dielectric rod. If a narrow strip is placed on the rod’s backside, it demonstrates a sharp growth of the near field at a certain high frequency. This is a combination of two effects. The first is the nonresonant optical effect called the photonic jet, and the second is the strip plasmon resonance. We would like to emphasize that our results have been computed with the aid of the convergent numerical method and have an accuracy of 10^{-6} or better in the near-field data.

We believe that the reported effect can be potentially useful for enhancing the imaging characteristics of THz systems. Besides, it can be used for the additional enhancement of the local field in the jet domain that can be attractive in the design of more sensitive THz receivers.

ACKNOWLEDGMENTS

This work was supported by the Ministry of Foreign and European Affairs, France and the Ministry of Education and Science, Ukraine, in the framework of the Program “Dnipro” that is acknowledged with gratitude.

REFERENCES

- B. S. Luk’yanchuk, R. Paniagua-Domínguez, I. Minin, O. Minin, and Z. Wang, *Opt. Mater. Express* **7**, 1820 (2017).
- A. Heifetz, S.-C. Kong, A. V. Sahakian, A. Taflove, and V. Backman, *J. Comput. Theor. Nanosci.* **6**, 1979 (2009).
- S. Lecler, S. Perrin, A. Leong-Hoi, and P. Montgomery, *Sci. Rep.* **9**, 4725 (2019).
- V. Pacheco-Peña and M. Beruete, *J. Appl. Phys.* **125**, 084104 (2019).
- V. R. Dantham, P. B. Bisht, and C. K. R. Nambodiri, *J. Appl. Phys.* **109**, 103103 (2011).
- Y. E. Geints and A. A. Zemlyanov, *J. Appl. Phys.* **119**, 153101 (2016).
- H. S. Patel, P. K. Kushwaha, and M. K. Swami, *J. Appl. Phys.* **123**, 023102 (2018).
- B. Vasic, G. Isic, and R. Gajic, *J. Appl. Phys.* **113**, 013110 (2013).
- Q. V. Shapoval and A. I. Nosich, *J. Phys. D Appl. Phys.* **49**, 055105 (2016).
- A. P. Anyutin, I. P. Korshunov, and A. D. Shatrov, *J. Commun. Technol. Electron.* **61**, 607 (2016).
- G. W. Hanson, *J. Appl. Phys.* **103**, 064302 (2008).
- M. Jablan, H. Buljan, and M. Soljacic, *Phys. Rev. B* **80**, 245435 (2009).
- A. Fallahi and J. Perruisseau-Carrier, *Phys. Rev. B* **86**, 195408 (2012).
- M. Yasir, P. Savi, S. Bistarelli, A. Cataldo, M. Bozzi, L. Perregrini, and S. Bellucci, *IEEE Antennas Wirel. Propagat. Lett.* **16**, 2380 (2017).

- ¹⁵W. Fuscaldo, P. Burghignoli, P. Baccarelli, and A. Galli, *Int. J. Microw. Wirel. Technol.* **9**, 1293 (2017).
- ¹⁶O. V. Shapoval, J. S. Gomez-Diaz, J. Perruisseau-Carrier, J. R. Mosig, and A. I. Nosich, *IEEE Trans. Terahertz Sci. Technol.* **3**, 666 (2013).
- ¹⁷T. L. Zinenko, *J. Opt.* **17**, 055604 (2015).
- ¹⁸V. Gerasik, M. S. Wartak, A. V. Zhukov, and M. B. Belonenko, *Mod. Phys. Lett. B* **30**, 1650185 (2016).
- ¹⁹M. E. Kaliberda, L. M. Lytvynenko, S. A. Pogarsky, and M. P. Roiuk, *Int. J. Microw. Wirel. Technol.* **11**, 326 (2019).
- ²⁰T. Oguzer, A. Altintas, and A. I. Nosich, *J. Eur. Opt. Soc.* **13**, 16 (2017).
- ²¹T. L. Zinenko, A. Matsushima, and A. I. Nosich, *IEEE J. Sel. Top. Quantum Electron.* **23**, 4601809 (2017).
- ²²M. Riso, M. Cuevas, and R. A. Depine, *J. Opt.* **17**, 075001 (2015).
- ²³E. A. Velichko, *J. Opt.* **18**, 035008 (2016).
- ²⁴M. Naserpour, C. J. Zapata-Rodríguez, S. M. Vuković, H. Pashaeiadi, and M. R. Belić, *Sci. Rep.* **12**, 12186 (2017).
- ²⁵V. I. Fesenko, V. I. Shcherbinin, and V. R. Tuz, *J. Opt. Soc. Am. A* **35**, 1760 (2018).
- ²⁶C. Valencia, M. A. Riso, M. Cuevas, and R. A. Depine, *J. Opt. Soc. Am. B* **34**, 1075 (2017).
- ²⁷A. P. Anyutin, I. P. Korshunov, and A. D. Shatrov, *J. Commun. Technol. Electron.* **63**, 815 (2018).
- ²⁸S. V. Dukhopelnykov, in *Proceeding of International Conference on Mathematical Methods in Electromagnetic Theory* (IEEE, 2018), p. 87.
- ²⁹S. V. Dukhopelnykov, in *Proceeding of International Seminar/Workshop DIPED* (IEEE, 2018), p. 51.
- ³⁰A. V. Kostenko, *Ukr. Math. J.* **65**, 1373 (2014).
- ³¹A. I. Nosich, T. Shiraishi, and Y. Okuno, *Rad. Sci.* **31**, 1733 (1996).